Journal of Alloys and Compounds 509 (2011) 8493–8500

Contents lists available at ScienceDirect

Journal of Alloys and Compounds

journal homepage: www.elsevier.com/locate/jallcom

# Absorption–emission study of hydrothermally grown Al:ZnO nanostructures

N. Rajeswari Yogamalar, A. Chandra Bose*

*Nanomaterials Laboratory, Department of Physics, National Institute of Technology, Tiruchirappalli 620 015, India*

ARTICLE INFO

*Article history:*
Received 7 December 2010
Received in revised form 25 May 2011
Accepted 3 June 2011
Available online 21 June 2011

*Keywords:*
Hydrothermal growth
Aspect ratio
Hexagonal wurtzite structure
Lattice vibration
Zinc vacancy

ABSTRACT

The preparation, structural characterization and optical properties of aluminum doped ZnO (Al:ZnO) nanostructures grown under hydrothermal method are reported. One-dimensional (1-D) growth is achieved by the controlled addition of metal nitrate as precursors in the presence of long chain surfactant, poly-ethylene glycol (PEG) at 160 °C for 20 h. The as-synthesized ZnO rods are single crystalline, exhibiting an oriented growth along [001] direction. The Al6 rod has an aspect ratio of 3.2, which can be effectively applied in optoelectronic devices. Comprehensive structural analysis using X-ray diffraction method (XRD) and Energy dispersive X-ray analysis (EDX) indicate that the dopant Al atom occupies Zn sites in ZnO and the elemental composition of Al is consistent with the amount utilized in the hydrothermal synthesis. XRD shows that the Al:ZnO nanostructures from 1 to 9 atomic percent (at.%) has hexagonal wurtzite structure of ZnO. The Al dopant effects on lattice vibration and electronic transitions of the ZnO nanostructures have been investigated by Fourier transform Infrared spectroscopy (FT-IR), Ultraviolet–visible (UV–vis) absorption spectroscopy and photoluminescence (PL) emission recorded at room temperature. The correlation existing between absorption and emission study tell that their characteristic band edge peak of doped ZnO shifts towards higher wavelength side for 3–9 at.% with respect to Al0 thus, exhibiting a red shift phenomenon with decrease in optical bandgap. The observed PL reveals two emission peaks centered at 374 nm and 530 nm. The near band edge (NBE) to defect emission ratio increases with dopant concentration indicating the linear enhancement in crystal quality and declination in zinc vacancies from 3 to 9 at.% of Al.

## 1. Introduction

ZnO is II–VI inorganic compound semiconductor, exhibiting a wurtzite structure with hexagonal unit cell ($P6_3mc$) [1–3]. The current theoretical and experimental work in the nano-field is much concerned in reporting a material with enhanced properties. To achieve such material compound significant conditions are adopted and analyzed thoroughly from the initial synthesis stage to device fabrication. The characteristic feature which decorates the nanocrystalline field or which lay a boundary between the discrete and continuum crystalline compound is the quantum confinement (QC) [4]. The QC plays a critical role in deciding the material properties and thereby exhibits an extraordinary performance. The performance is further enriched and manipulated by several factors such as establishing appropriate growth technique, having a control on the synthesis condition, tuning the distribution and concentration of atom, selective incorporation of foreign atoms and many more. Among them, the widely accepted method to modify the electrical and optical properties of a semiconductor is the addition of impurity atoms or doping [5–7].

The crystal structure and optical properties of ZnO are more similar to that of GaN [8]. ZnO is *n*-type semiconductor with wide bandgap of 3.37 eV and large exciton binding energy of 60 meV at room temperature, makes it a potential candidate for technological applications in photo detectors, LED's and laser diodes [9,10]. The introduction of dopant atom into the ZnO lattice sites can significantly influence the optical, electrical and magnetic properties, as they affect the electronic band structures and optoelectronic properties [11–13]. Few transition metal ions doped ZnO nanocrystals are cited for reference. ZnO has been doped with Mn or rare earth elements [14,15] in order to change their luminescence properties. The electrical and optical properties of ZnO are enhanced by doping with group III, IV, and V elements (e.g. Li, Ga, In, Sn, Sb, N, and P) [16–20]. Spintronic devices such as magnetic-optic switches, magnetic sensors, spin valve transistors, spin light emitting diodes can be activated by implanting ferromagnetic Mn, Ni, Co and Cr in ZnO nanorods [21–24]. Aluminum doping induces superior conducting properties based on vacancies. As a result, Al-doped ZnO has been considered as transparent conducting oxides (TCO) and piezoelectric (PZT) materials for fabricating solar cells, electrodes, high electron mobility transducers and gas sensors [25–30]. The enriched conductivity in Al-doped ZnO is regarded as an alternative candidate for indium tin oxide (ITO) materials. The solution-route assisted rapid thermal annealing (RTA) process referred in paper

---

* Corresponding author. Tel.: +91 9444065746; fax: +91 431 2500133.
*E-mail address:* acbose@nitt.edu (A. Chandra Bose).

0925-8388/$ – see front matter © 2011 Elsevier B.V. All rights reserved.
doi:10.1016/j.jallcom.2011.06.012

[31,32] reports the fabrication of 1-D, 2-D and 3-D nanoarchitectures without the use of template and seed nuclei and its influence in enhancing the optical properties.

In this paper, the structure, absorption and emission study of Al:ZnO grown under hydrothermal method with different concentrations of Al have been evaluated. Al behaves as a donor and modifies the luminescence emission in ZnO by creating localized impurity level. Usually, the substitution of impurity atom into the host lattice is hindered by an increase in surface energy and lattice distortion. In consideration of high energetic potential, a suitable chemical synthesis method with optimized parameters is required to incorporate the dopant atoms into the host lattice. Here, we utilized a hydrothermal growth performed at 160 °C for 20 h towards the synthesis of Al:ZnO. The doping level is adjusted during the synthesis and a high doping concentration up to 15 at.% is achieved and characterized systematically. The correlation between absorption and emission study of Al:ZnO illustrates a significant implementation in optoelectronic devices.

## 2. Experimental procedure

### 2.1. Materials and method

The ZnO nanostructures are prepared through hydrolysis of zinc nitrate hexahydrate and for Al:ZnO, aluminum nitrate nonahydrate are used as dopant precursor. $Zn(NO_3)_2{\cdot}6H_2O$, $Al(NO_3)_3{\cdot}9H_2O$, PEG with 98% purity are utilized as received condition. Throughout the synthesis the double distilled water is used for aqueous solution preparation.

Here, a solution mixture of 0.1 M host precursor $Zn(NO_3)_2$ and dopant precursor $Al(NO_3)_3$ in appropriate atomic percent is used to synthesize pure and doped ZnO. A surfactant solution of 0.1 mM PEG is prepared and dissolved into the precursor solution. After stirring for 60 min, ammonia solution is added drop-wise until the pH attains 7–8. The obtained white precipitate is allowed to settle and 80 ml of the solution mixture is transferred into teflon lined stainless steel autoclave of 100 ml capacity and heated at 160 °C for 20 h to incorporate the dopant ion. The resulting white precipitate is centrifuged with ethanol and distilled water repeatedly. Finally, the precipitate is dried at room temperature and collected for various characterizations. The influence of dopant on the structure, morphology and optical properties of ZnO is recognized by varying the dopant concentration from 0 to 15 at.%. The as-synthesized $Zn_{1-x}Al_xO$ sample products are designated as Al*X* where, *X* is the dopant concentration numbered as 0, 1, 3, 6, 9 and 15 in at.%.

### 2.2. Characterization tools

The as-grown sample materials ($Zn_{1-x}Al_xO$) are structurally characterized and analyzed by scanning electron microscopy (SEM) equipped with EDX, transmission electron microscopy (TEM), high resolution TEM (HRTEM) and powder XRD. The surface morphology, the chemical composition and dopant concentration are examined using Hitachi S4800 FESEM integrated with EDX. For TEM and electron diffraction analysis, Jeol JEM FX II 2000 operating at 200 kV is used to examine the morphology of the pure and doped ZnO. XRD spectra are recorded using Ultima III Rigaku powder X-ray diffractometer with Cu $K_{\alpha 1}$ source ($\lambda$ = 1.5406 Å) in $\theta$–$2\theta$ configuration. In X-ray analysis the loose sample powder is leveled in the sample holder to ensure a smooth surface and mounted on a fixed horizontal sample plane. The optical properties including optical absorbance and emission of pure and Al:ZnO are measured using spectrometer. Room temperature optical spectra in the UV and visible light wavelength ranges are recorded using Shimadzu UV-1700 Pharma spectrophotometer. In the UV–vis absorption measurement $Zn_{1-x}Al_xO$ precipitate is dispersed and the spectrophotometer measures the absorbance, relative to the standard powder of $BaSO_4$. The emission spectra are recorded in Shimadzu (RF-5301 PC) spectrofluorophotometer under an excitation wavelength of 230 nm using 150 W Xenon lamp. FT-IR spectra of Al0 and Al6 mixed with the white standard KBr pellet are recorded using Perkin-Elmer FT-IR spectrometer in the range of 4000–400 $cm^{-1}$.

## 3. Results and discussion

### 3.1. Micrograph analysis

The FESEM studies depicted in Fig. 1a–d indicate that the morphology of hydrothermally grown ZnO and Al:ZnO are rod shaped. Fig. 1a and b shows the FESEM images of ZnO nanorods derived from $Zn(NO_3)_2$ precursor. Particles are found as agglomerates and bundles of ZnO nanoparticles are observed. Here, four to six short ZnO nanorods are grouped to form a single bundle. The bundle comprises of ZnO nanorods with varying length and diameter thus, showing uneven and wide size distribution. Few rods are found to be separated and oriented randomly. The end of the rod is hexagonal in shape. The formation of nano-bundles with short rods indicates that the nucleation is rapid while, the particle growth is highly inhibited. Because of this the crystallite size of Al0 is comparatively smaller than Al6. No definite size and shape of the particles can be described from SEM micrographs as they are highly aggregated. The morphology of hydrothermally grown Al6 is displayed in Fig. 1c and d. From the high magnified FESEM image (Fig. 1d), one can observe that the Al6 is rod shaped with homogeneous diameter over the entire particle. The typical length of the rod is in micron scale ranging from 1 to 2 μm and the diameter is about 900 nm. Apart from rods, particles of varying size are also found in the micrograph and this predicts an incomplete or heterogeneous nucleation of the particle. The micrograph result is consistent with the earlier reported paper [33].

The elemental composition of the as-synthesized Al0 and Al6 are carried out using EDX integrated with SEM instrument as predicted in Fig. 1e and f. From EDX measurements, the presence of Zn, O and Al and their compositions are determined. The percentage calculation of Al in Al6 is consistent with the percentage of dopant atom taken during the sample preparation. Thus, EDX measurements confirm that the Al dopant is substituted for Zn and its composition is 1.04 at.% of total metal elements in Al6. Zn, Al and O are not in stoichiometric ($Zn_{0.95}Al_{0.05}O$) and Zn is found to be in excess. The other signals originate from the carbon coated grid. In mechanism, the substitution of $Al^{3+}$ ions for $Zn^{2+}$ in ZnO lattice results in one extra electron thus; it produces *n*-type impurity. However, in order to maintain charge neutrality the intrinsic defects are produced simultaneously. For example substitution of two $Al^{3+}$ ions replaces two $Zn^{2+}$ ions and creates one zinc vacancy as a consequence of stoichiometric. This outcome is also evident from the Zn/O ratio measurement from EDX. For Al0, the Zn/O ratio is 1.45 whereas in Al6, the ratio is 0.83 due to the creation of excess zinc vacancies.

The TEM and SAED pattern provide a detailed study on the microstructure and growth direction of ZnO nanostructures. TEM micrographs of as-prepared Al0 and Al6 are shown in Fig. 2a and b and their corresponding SAED pattern are shown as an inset. Fig. 2a is the TEM micrographs of ZnO consisting of highly short and irregular nanorods of varying length and diameter. As the particle growth is highly inhibited, the surface to volume ratio is increased with increase in surface activation energy thereby, bringing the particle closer and binding them together to form a bundle of indefinite shape and size as seen from their SEM images in Fig. 1a and b. The TEM also confirms that the end of Al0 nanorods is hexagonal in nature and their aspect ratio is 2.30. The SAED pattern indicates that the ZnO nanostructure is single crystalline with preferred [001] growth direction. Fig. 2b is the TEM micrograph of Al6 comprising of single rod in micron range. The diameter of the rod is about 90 nm and this value is inconsistent with the one obtained from SEM micrograph (Fig. 1c and d). As the low magnified SEM micrographs shown in Fig. 1c comprises of both rods of varying size and particle, the region focused in TEM image may be particle consisting of rods with low diameter. The SAED pattern of Al6 nanostructure displays a distributed dotted pattern, assigning to crystalline nature.

### 3.2. Phase confirmation

The phase purity and crystal structure of the pure and doped ZnO nanostructures have been analyzed by XRD and Fig. 3a shows the XRD pattern of pure and Al:ZnO grown by hydrothermal method. As we can see, the samples with dopant concentration ≤9 at.% crystallizes in single phase and can be indexed to hexagonal wurtzite type ZnO (JCPDS ID: 36-1451). But, with higher doping concentra-

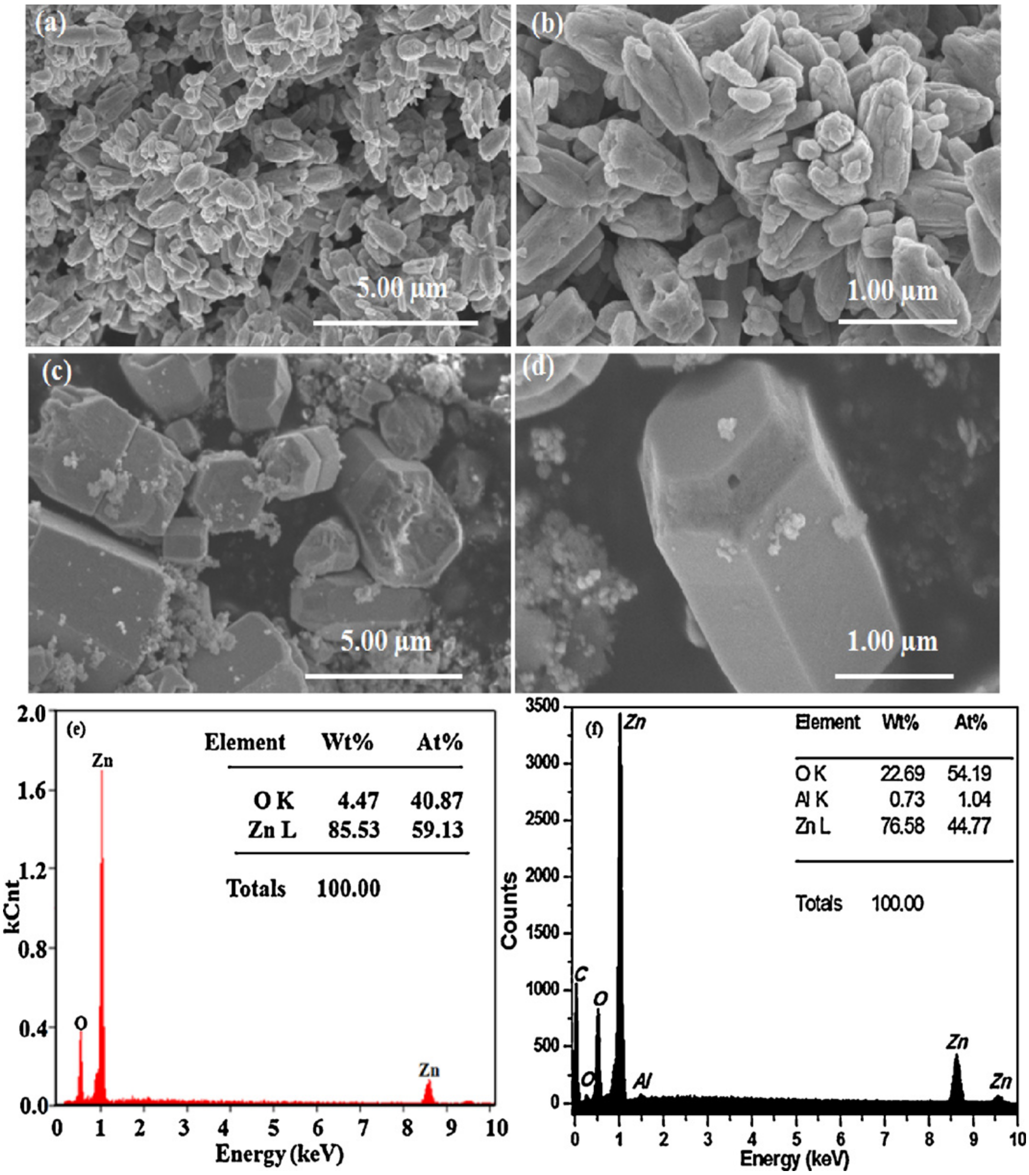

(e)

| Element | Wt% | At% |
|---|---|---|
| O K | 4.47 | 40.87 |
| Zn L | 85.53 | 59.13 |
| Totals | 100.00 | |

(f)

| Element | Wt% | At% |
|---|---|---|
| O K | 22.69 | 54.19 |
| Al K | 0.73 | 1.04 |
| Zn L | 76.58 | 44.77 |
| Totals | 100.00 | |

**Fig. 1.** FESEM micrographs of hydrothermally grown (a–b) pure (Al0), (c–d) doped ZnO (Al6), and (e–f) EDX spectra of Al0 and Al6 respectively.

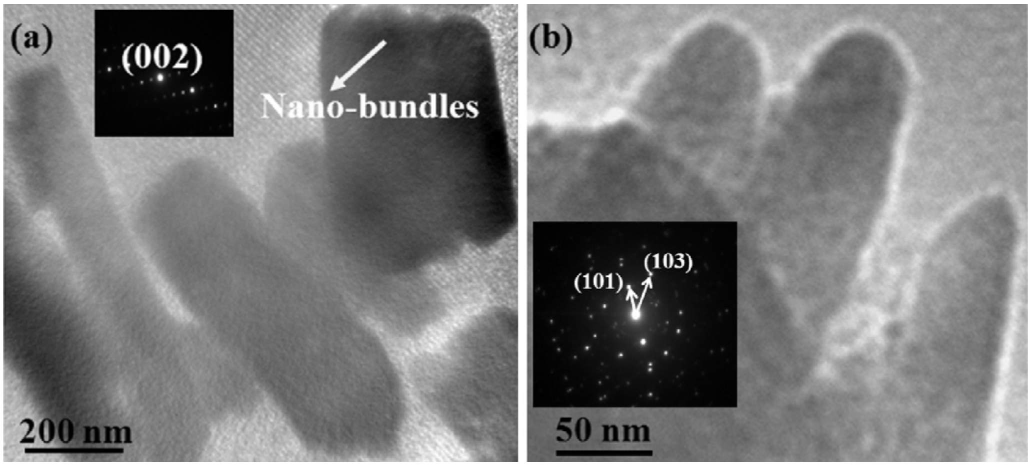

**Fig. 2.** TEM images of pure and Al6 nanostructures and the inset show their corresponding electron diffraction pattern.

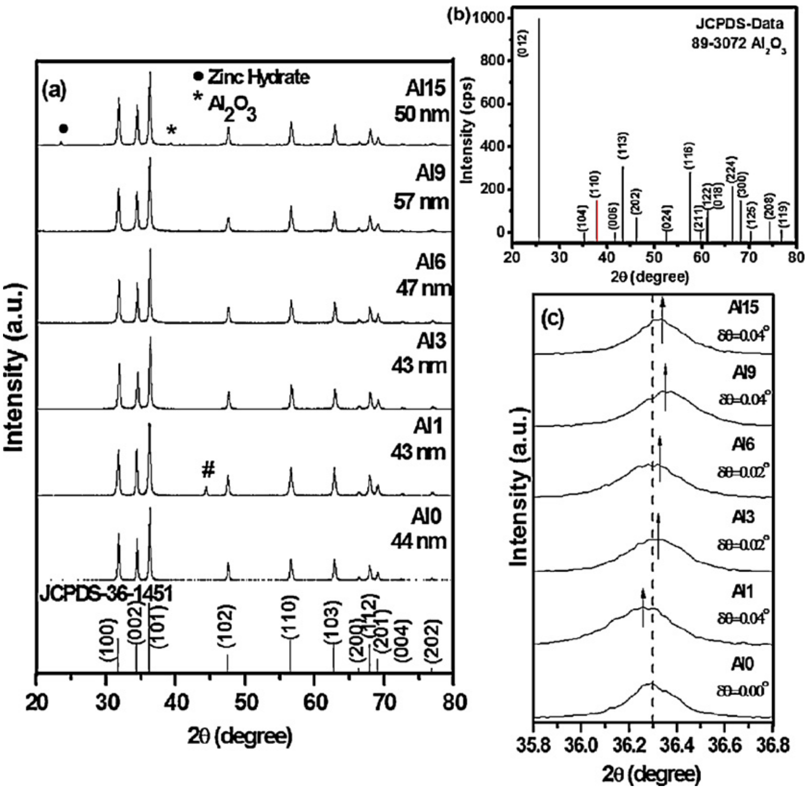

**Fig. 3.** (a) XRD powder diffraction pattern of $Zn_{1-x}Al_xO$ ($x = 0, 1, 3, 6, 9$, and 15 at.%) nanostructures, (b) JCPDS data file of $Al_2O_3$, and (c) Changes in the (101) peak position with Al concentration.

tion (>9 at.%) the crystallinity decreases and impurity secondary phase peak corresponding to $Al_2O_3$ and hydroxyl group of Zn–O are observed at $2\theta = 23^\circ$ and $2\theta = 39^\circ$ (marked as •, * in Fig. 3a). For better comparison and to represent the phase purity of the sample, standard JCPDS database of $Al_2O_3$ is included in Fig. 3b. The symbol # is used to denote the sample holder peak at $2\theta = 44^\circ$. The strongest diffraction peak near 34° is from the ZnO (101) plane. Several other peaks corresponding to (100), (002), (102), (110), and (103) planes of ZnO are also present. It indicates that the rod formed in Al:ZnO are single crystalline with different orientations. Moreover, the variation in intensity (not included in figure) of (101) peak concludes that the degree of crystallinity is changed due to the incorporation of Al atom. The substitution of dopant Al atom into the host lattice ZnO is confirmed from the angle shift $\delta(2\theta)$ for the strongest peak of ZnO (101) reflection as a function of the doping concentration in at.% is illustrated in Fig. 3c. $\delta(2\theta)$ shifts to lower angle as $x$% increases from 0 to 1 at.%, but monotonically and significantly shifts to higher angle up to 15 at.%. The shift in peak position towards the higher angle clearly demonstrates the effective substitution of $Al^{3+}$ for $Zn^{2+}$ ions and is in concurrent with Vegard's law. Further, the confirmation is made from the measurement of lattice parameters '$a$' and '$c$'. The decrease in lattice parameters can be accounted to the substitution of smaller $Al^{3+}$ (0.535 Å) in place of $Zn^{2+}$ (0.74 Å) in tetrahedral coordination of ZnO wurtzite structure [34]. However the peak intensity varies with doping concentrations indicating the lattice distortion and the crystalline quality due to the introduction of dopant atoms. The average crystallite size is calculated from the XRD pattern using the well known Scherrer formula [35] (Eq. (1)) with the integral widths corrected with standard Si sample (Eq. (2)) using Cauchy–Lorentzian fit. For crystalline size analysis, the high intense (101) reflection of the hexagonal phase ZnO is employed.

$$R = \frac{0.9\lambda}{\beta_{hkl} \cos \theta} \tag{1}$$

where, $R$ is the average crystallite size, $\lambda$ is the Cu $K_{\alpha 1}$ radiation of wavelength 1.5406 Å, $\beta_{hkl}$ is the instrumental corrected full width at half maximum in radians and $\theta$ the scattering angle in degree. The corrected instrumental broadening for Lorentzian fit is given by

$$\beta_{hkl} = \beta_{\text{measured}} - \beta_{\text{instrumental}} \tag{2}$$

It is found that the crystallite size initially decreases to 43 nm for Al1 and Al3 samples in comparison to Al0 (44 nm) sample. Later with increase in Al concentrations the crystallite size increases and reaches its maximum at 57 nm for Al9 sample and then decreases. Fig. 4a and b portrays the error graph in lattice parameters, crystallite size, and peak shift as a function of dopant concentration.

### 3.3. Strain analysis

A mathematical expression relating the crystallite size and strain induced broadening is proposed by Williamson and Hall. According to the expression, the peak width as a function of diffraction angle $2\theta$ is considered for analyzing X-ray peak broadening [36,37]. The relation is defined as

$$\beta_{hkl} \cos \theta = \left(\frac{C\lambda}{R}\right) + (2\varepsilon \sin \theta) \tag{3}$$

where, $C$ is a shape factor taken as 0.9 and $\varepsilon$ is the strain induced on the particle. A plot shown in Fig. 4c is drawn with $\sin\theta/\lambda$ along $x$-axis and $\beta_{hkl} \cos\theta/\lambda$ along $y$-axis for diffraction peak lying in the range of 20°–60°. From the linear fit to the data, the average crystallite size and strain of $Zn_{1-x}Al_xO$ are extracted from the inverse of the intercept at the $y$-axis and slope respectively. A trend line is drawn to illustrate the deviation of the data points from the linear fit. This deviation reveals the anisotropic nature of the crystal and wide size distribution. The average crystallite size and strain estimated from the Scherrer formula and W–H plot are compared and tabulated in Table 1. From the table, one can reveal that the

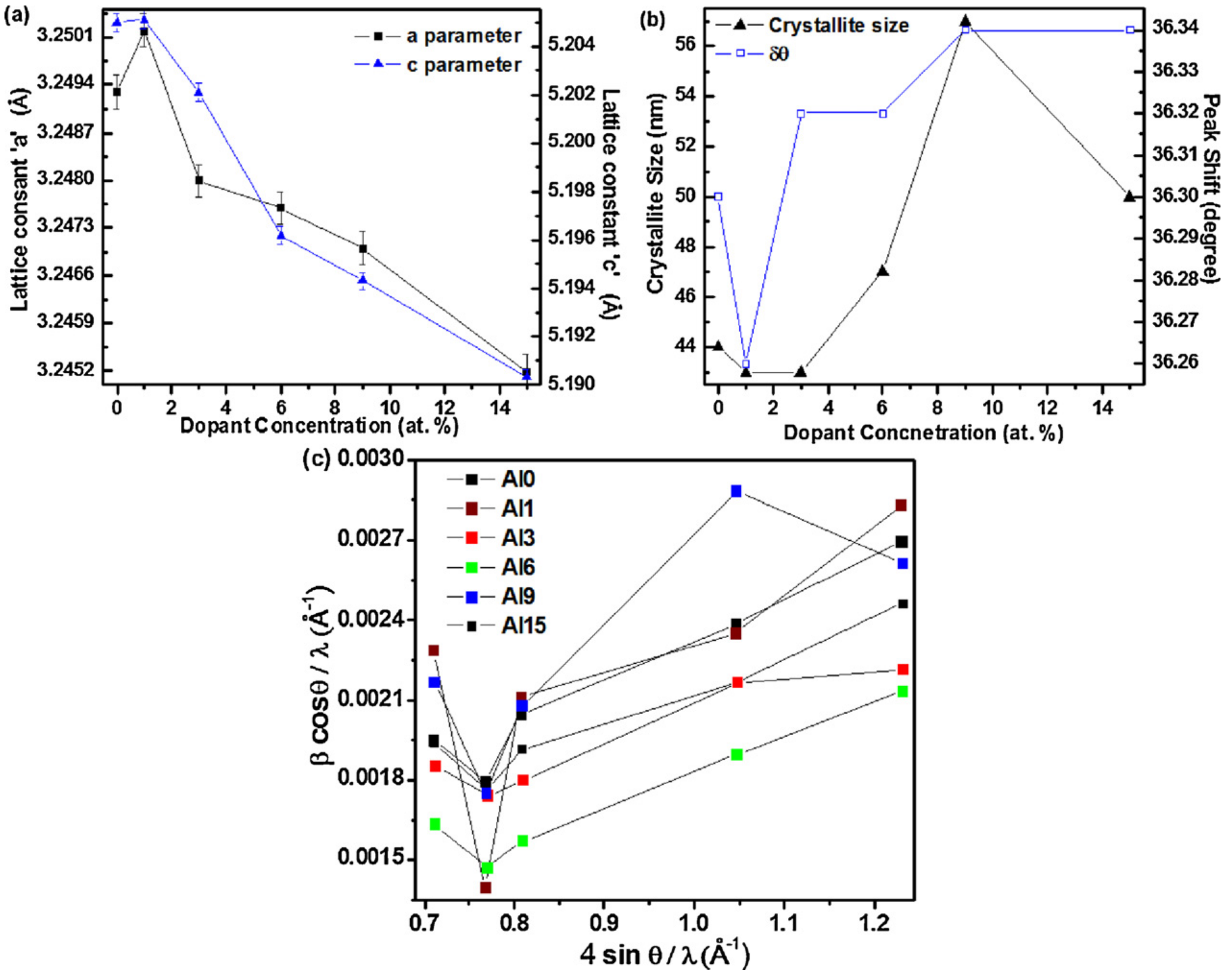

**Fig. 4.** (a) Variation in the lattice parameters '*a*' and '*c*'; (b) the shift in peak position ı(2) and the crystallite size variation; and (c) W–H plot of wurtzite hexagonal phase ZnO as a function of dopant concentration.

**Table 1**
Geometric parameters of pure and Al:ZnO nanostructures.

| Samples | Scherrer relation | W–H plot | Lattice parameters | Volume | | |
|---|---|---|---|---|---|---|
| | Crystallite size *R* (nm) | Crystallite size *R* (nm) | Strain ε (no unit) | '*a*' (Å) | '*c*' (Å) | (Å$^3$) |
| Al0 | 44 | 126 | 0.00160 | 3.2493 | 5.2050 | 47.592 |
| Al1 | 43 | 143 | 0.00172 | 3.2502 | 5.2051 | 47.619 |
| Al3 | 43 | 107 | 0.00160 | 3.248 | 5.2021 | 47.528 |
| Al6 | 47 | 132 | 0.00167 | 3.2476 | 5.1962 | 47.461 |
| Al9 | 57 | 134 | 0.00117 | 3.2470 | 5.1943 | 47.427 |
| Al15 | 50 | 82 | 0.00119 | 3.2452 | 5.1903 | 47.337 |

average crystallite size estimated from Scherrer relation and W–H plot are dissimilar. The vast difference in crystallite size calculation is mainly attributed to the inclusion of strain in the as-synthesized sample and their estimated strain values are reasonable. Thus, W–H plot serves as an additional tool to evaluate and deconvolute the crystallite size and strain induced broadening. The strain due to lattice dislocation is associated with defect emission observed in PL (discussed in Section 3.5).

### *3.4. Absorption study*

In optical absorption, electrons are excited from the valence band to the conduction band. The changes in absorption spectra for ZnO doped with various concentration of Al are characterized by means of UV–vis absorption spectroscopy. Fig. 5a displays the UV–vis absorption spectra of pure and Al:ZnO nanostructures measured at room temperature. In Fig. 5a as the ZnO nanostructures are doped with Al, the absorption curve of the UV–vis absorption spectra shifts to higher wavelength side for 3–9 at.% with reference to Al0. The inset of Fig. 5a shows the plot for estimating the onset of absorption of Al3. Extrapolating the linear portion and knee portion, the onset of absorption is determined from their point of intersection. The UV peaks of Al0, Al1, Al3, Al6, Al9, and Al15 are located at 394 nm, 387 nm, 395 nm, 397 nm, 407 nm, and 400 nm, respectively. The red shift of 20 nm (407–387 nm) for 3–9 at.% Al:ZnO nanostructures indicate a reduction of ZnO bandgap caused by the Al doping. The onset of absorption increases with Al concentration (3–9 at.%) in the ZnO nanostructures, as illustrated in Fig. 5c. It gives a direct evidence for the narrowing of optical bandgap.

The relation between the absorption coefficient $\alpha$ and the incident photon energy $h\nu$ can be written as

$$\alpha h\nu = (A(h\nu) - E_g)^n \qquad (4)$$

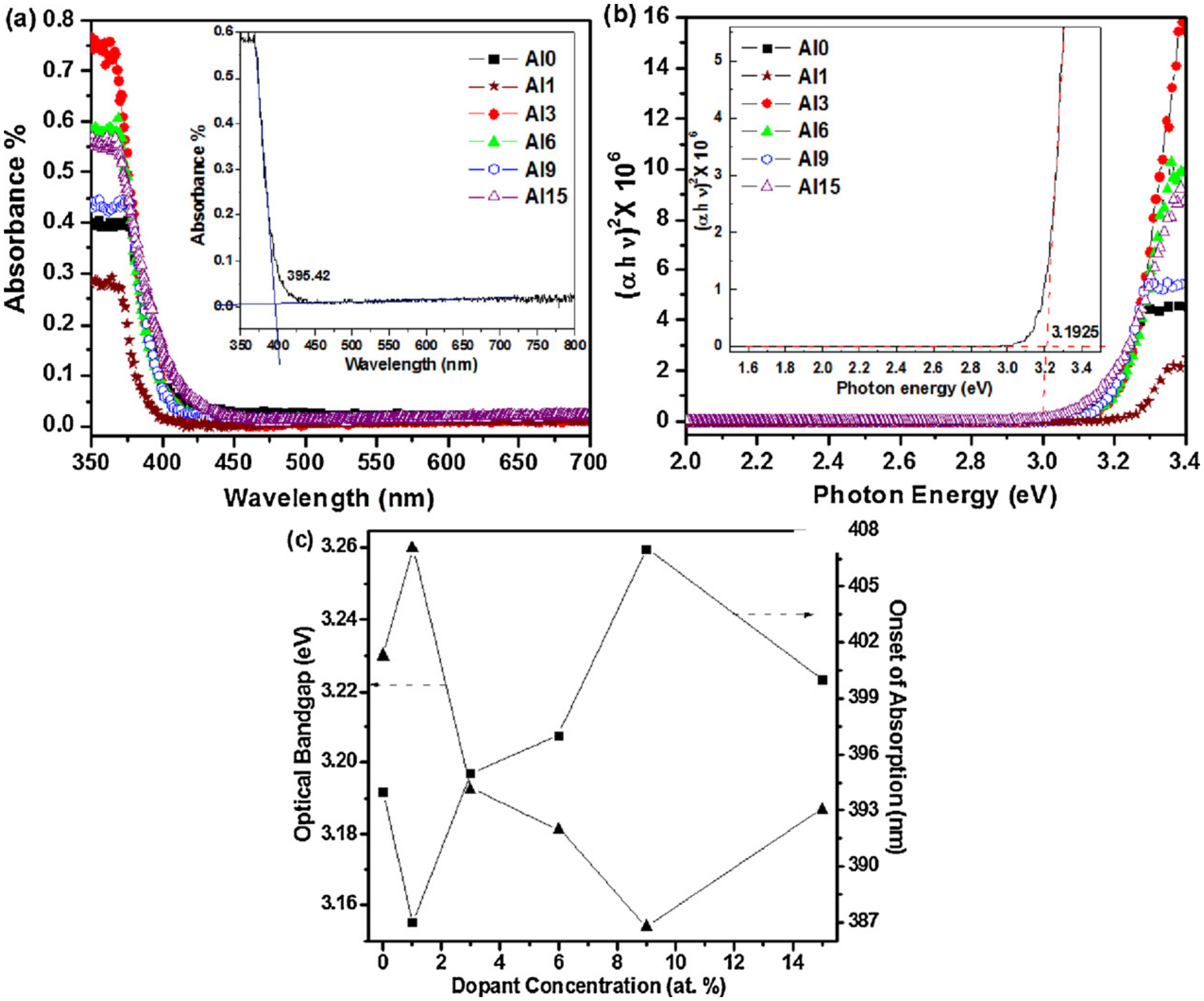

**Fig. 5.** (a) UV absorption spectra of $Zn_{1-x}Al_xO$ ($x$ = 0, 1, 3, 6, 9, and 15 at.%) and the inset shows the point of intersection measured for Al3, (b) Tauc plot relation and the inset show the bandgap estimation for Al3, and (c) change in onset of absorption and optical bandgap energy as a function of Al percent.

where $E_g$ is the optical bandgap, $A$ is the constant, and the exponent $n$ depends on the type of transition [38]. The $n = 1/2$ for allowed direct transition, 2 for allowed in-direct transition, 3/2 and 3 for forbidden direct and forbidden indirect transitions respectively. Considering direct band transition in ZnO, a plot between $(\alpha h\nu)^2$ versus photon energy $h\nu$ is drawn for various Al dopant concentrations as shown in Fig. 5b and their inset shows the method adopted to estimate the bandgap value of Al3. From the point of intersection, the direct bandgap is found to be 3.23 eV, 3.26 eV, 3.19 eV, 3.18 eV, 3.15 eV, and 3.18 eV for Al0, Al1, Al3, Al6, Al9 and Al15 respectively as estimated from Fig. 5c. The narrowing of the bandgap in heavily doped semiconductor can be reasoned out by many factors. The prime contributions are increase in crystallite size, impurity band formation, band–band transition due to various defects, bandgap bowing effect, and many more [39]. In our experimental work, the bandgap narrowing observed in Al:ZnO (3–9 at.%) is purely subjected to variation in crystallite size due to Al incorporation. Thus, a red shift phenomenon is exhibited, where the Al doping results in decrease in optical bandgap deviating from the Burstein–Moss shift [40,41]. The estimated bandgap values are close to that of bulk ZnO. This gives a conclusion that there is no indication of quantum size confinement. The bandgap of Al:ZnO nanostructures shows a non-monotonic dependence on the Al concentration, as depicted in Fig. 5c. The bandgap increases initially for Al1 sample in contrast to Al0 as their crystallite size is smaller than Al0. Then the bandgap value reaches a minimum value at 9 at.% of Al, and then increases. Thus, the observation of non-monotonic behavior in the bandgap of a ZnO nanocrystal as a function of the Al content strongly supports that Al is indeed localized into the host lattice of ZnO.

### 3.5. *Emission study*

The emission spectra recorded at room temperature are shown in Fig. 6a for various concentrations of Al:ZnO nanostructures excited at 230 nm. The PL spectra of doped ZnO is composed of two emission peak, including a strong NBE emission centered at 373 nm (3.33 eV) in the UV region and a weak green emission centered at 530 nm (2.34 eV) in the visible region as illustrated in Fig. 6a. The UV peak corresponds to the radiative recombination of free excitons of ZnO and the green peak is related to the radiative recombination of a photo-generated hole with an electron occupying the doubly ionized zinc vacancy [42–44]. The green luminescence from the surface defect sites with a maximum around 530 nm is observed only for the doped samples and this is attributed to the introduction of defects with dopant incorporation [45]. The dominance of green emission in doped ZnO compared to that of pure ZnO is due to large charge density of $Al^{3+}$. This will give rise to more surface defects such as zinc vacancies and hence, enhance the green luminescence. The ratio of the emission intensity calculated between the NBE emission and defect emission is displayed as an inset in Fig. 6a. It is

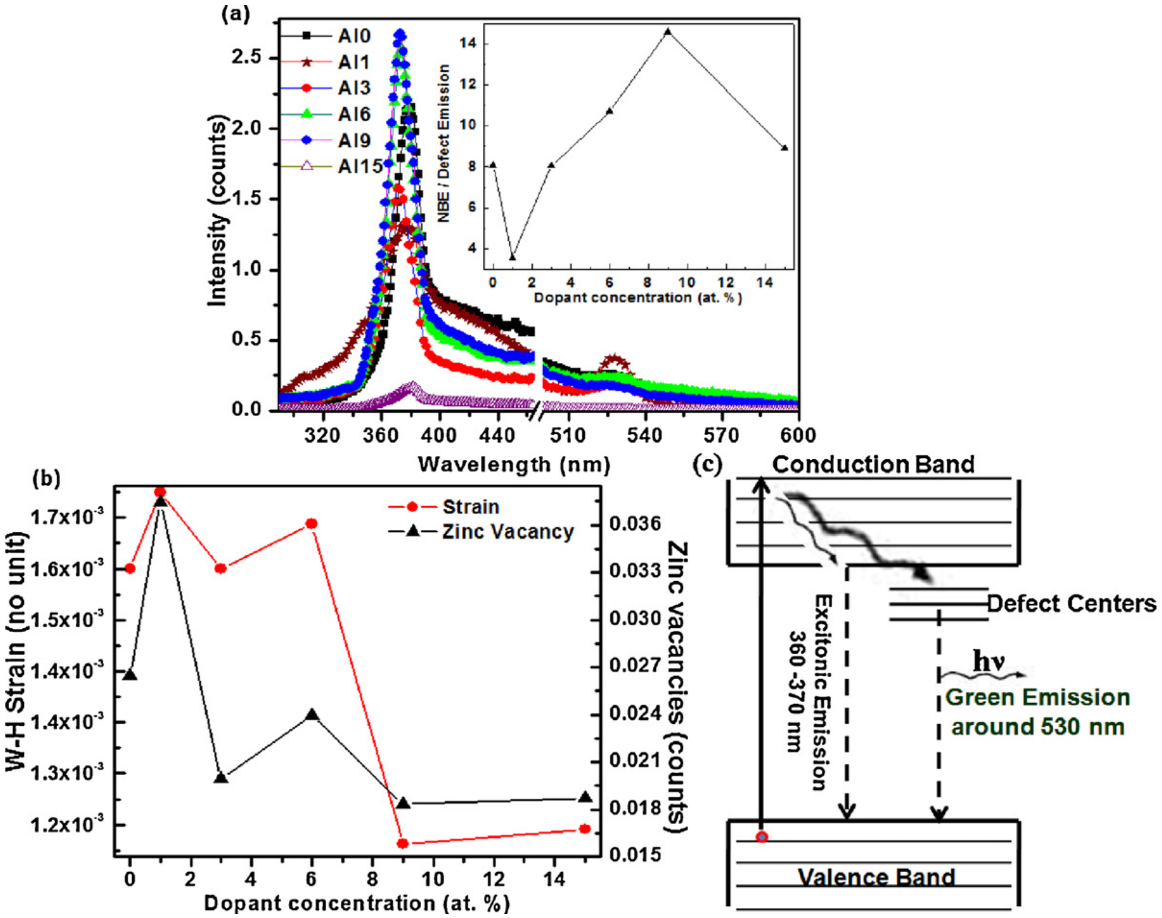

**Fig. 6.** (a) Room temperature luminescence spectra of $Zn_{1-x}Al_xO$ ($x = 0$, 1, 3, 6, 9, and 15 at.%) excited under the wavelength of 230 nm and the inset shows the intensity ratio between NBE and defect emission, (b) graph to show the relation existing between lattice strain and zinc vacancy concentration and (c) Schematic illustration of the luminescence emission associated with doped ZnO.

related to the degree of crystallinity and the density of zinc vacancies. In Al1, the defect emission is highly pronounced and hence they exhibit lower crystallinity in contrast to Al0. From the figure it is very obvious that there is an asymmetric variation in zinc vacancy with increase in dopant concentrations. The variation in NBE/defect emission (inset of Fig. 6a) exhibits a similar trend, as observed in the crystallite size variation and onset of UV absorption, predicted in Figs. 4b and 5c, respectively. Fig. 6b shows the variation in lattice strain and zinc vacancies as a function of dopant concentration. The figure clearly demonstrates that the origin of surface defects is due to the lattice dislocation as dopant atoms are introduced into the host lattice sites. Thus, the electronic transitions, the density of zinc vacancies, surface defects and their relation with structure property are remarkably decided by PL study. The schematic representation of various emissions associated with Al:ZnO nanoparticles is shown in Fig. 6c. Here, the electrons get trapped in the defect state established by zinc vacancy in the forbidden region and relaxes by radiation emission in the green visible region. The overall observations and measurements from UV–vis absorbance and PL spectrum are summarized in Table 2.

### *3.6. IR transmission spectra*

The transmission peaks recorded in an IR spectrum, serves as a fingerprint of a sample [39]. Each peak corresponds to the frequency of vibrations between the bonds of the atom making up the material. In addition, the broadening of the peaks in the spectrum is a direct indication of the size and crystallinity of the material compound. The formation of Al:ZnO powders and metal-oxide interaction are well identified from FT-IR study. Fig. 7 shows the FT-IR transmission spectra of Al0 and Al6 samples. The first and sharp intense peak at 430 $cm^{-1}$ can be assigned to the stretching mode of Zn–O [46]. When the dopant atoms are introduced, the vibration mode shifts towards the higher wavenumber side and is

**Table 2**
Optical measurements of $Zn_{1-x}Al_xO$ ($x = 0$, 1, 3, 6, 9 and 15 at.%) nanostructures.

| Samples | UV absorption spectra | | Luminescence spectra | | |
|---|---|---|---|---|---|
| | Onset of absorption (nm) | Optical bandgap energy (eV) | NBE emission (counts) | Zinc vacancy (counts) | W–H strain (no unit) |
| Al0 | 394 | 3.23 | 0.21402 | 0.02648 | 0.00160 |
| Al1 | 387 | 3.26 | 0.13301 | 0.03743 | 0.00172 |
| Al3 | 395 | 3.19 | 0.16041 | 0.01992 | 0.00160 |
| Al6 | 397 | 3.18 | 0.25626 | 0.02395 | 0.00167 |
| Al9 | 407 | 3.15 | 0.26771 | 0.01834 | 0.00117 |
| Al15 | 400 | 3.18 | 0.16657 | 0.01872 | 0.00119 |

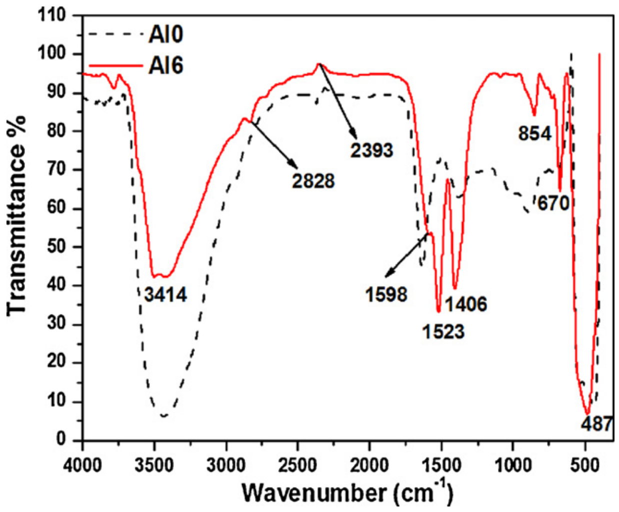

**Fig. 7.** FT-IR transmission spectra of pure ZnO and Al6 nanostructures.

located at 487 cm$^{-1}$. Moreover, the intensity of the vibration mode remains the same with the inclusion of Al atom. The broadening of the peak exhibited by Al0 and Al6 samples are almost similar, indicating both are crystalline with comparable crystallite size as shown in Table 1. A sharp distinct peak appears at 670 cm$^{-1}$ for Al6 sample and it is assigned as a fingerprint for Al–O. The –CH– stretching band belonging to the PEG block appear between 2300 and 2830 cm$^{-1}$ [47]. The transmittance at 1400 cm$^{-1}$ is assigned to the deformation of NH. The broad absorption in the frequency band 3000–3750 cm$^{-1}$ are assigned to O–H stretching from residual alcohols, water and Zn–OH bonds. The sharp absorption at 1600 cm$^{-1}$ in the higher frequency range is associated with the deformation vibration of H–O–H bonds of the physisorbed water. The shift in IR transmission spectrum of Al0 sample in contrast to Al6 sample is mainly ascribed to the crystal perturbation introduced by the dopant atom into the lattice sites.

## 4. Conclusions

In summary, the controlled doping has an extensive implications and effects on the crystalline and electronic structures of ZnO. Single crystalline Al:ZnO rods in micron scale is synthesized through simple hydrothermal method in the presence of PEG. The structural investigation with XRD and EDX proves the substitution of Al ions into the wurtzite Zn lattice sites. The difference in Zn/O ratio existing between Al0 and Al6 reveals the creation of zinc vacancy with dopant incorporation. It is worth to highlighting that the UV absorption is red shifted for 3–9 at.% Al:ZnO nanostructures, deviating from the usual bandgap widening explained on the basis of Burstein–Moss shift. The substitution of dopant atom into the Zn sites clearly demonstrates that the crystallinity is improved due to the reduction of surface defects and lattice distortions as evidenced from PL and XRD results. Thus, from the results of absorption and emission study, we suggest that the bandgap as well as the electronic transition properties of ZnO can be modified with controlled doping of Al.

## Acknowledgement

The research was funded by DST project (SR/FTP/ETA-31/07), Government of India.

## References

[1] Ü. Özgür, I.Y. Alivov, C. Liu, A. Teke, M.A. Reshchikov, S. Doğan, V. Avrutin, S.J. Cho, H. Morkoç, J. Appl. Phys. 98 (2005) 041301-103.
[2] A. Janotti, C.G. Van de Walle, Rep. Prog. Phys. 72 (2009) 126501–126529.
[3] H. von Wenckstern, H. Schmidt, M. Brandt, A. Lajna, R. Pickenhain, M. Lorenz, M. Grundmann, D.M. Hofmann, A. Polity, B.K. Meyer, H. Saal, M. Binnewies, A. Borger, K.D. Becker, V.A. Tikhomirov, K. Jug, Prog. Solid State Chem. 37 (2009) 153–172.
[4] M. Cahay, J.P. Leburton, D.J. Lockwood, S. Bandyopadhay, J.S. Harris, Quantum Confinement VI: Nanostructured Materials and Devices, The Electrochemical Society Inc., Pennington, NJ, USA, 2001.
[5] L.S. Hsu, C.S. Yeha, C.C. Kuob, B.R. Huangc, S. Dhar, J. Optoelectron. Adv. Mater. 7 (2005) 3039–3046.
[6] R.N. Bhargava, D. Haranath, A. Mehta, J. Korean Phys. Soc. 53 (2008) 2847–2851.
[7] S.Y. Bae, C.W. Na, J.H. Kang, J. Park, J. Phys. Chem. B 109 (2005) 2526–2531.
[8] V.A. Karpina, V.I. Lazorenko, C.V. Kopylova, V.A. Baturin, S.A. Pustovoytov, A. Ju, S.A. Eremin, P.M. Lytvyn, V.P. Ovsyannikov, E.A. Mazurenko, Cryst. Res. Technol. 39 (2004) 980–992.
[9] L. Luoa, Y. Zhang, S.S. Mao, L. Lin, Sens. Actuators A 127 (2006) 201–206.
[10] L.N. Demyanets, L.E. Li, T.G. Uvarova, M. Yu Mininzon, Inorg. Mater. 44 (2008) 40–44.
[11] M.C. Amann, F. Capasso, A. Larsson, M. Pessa, New J. Phys. 11 (2009) 125012–125015.
[12] W.W. Li, Z.G. Hu, J.D. Wu, J. Sun, M. Zhu, Z.Q. Zhu, J.H. Chu, J. Phys. Chem. C 113 (2009) 18347–18352.
[13] Y. Hu, Y. Chang, P. Fei, SnyderF R.L., Z.L. Wang, Nano 4 (2005) 1234–1240.
[14] T. Meron, G. Markovich, J. Phys. Chem. B 109 (2005) 20232–20236.
[15] W.W. Li, W.L. Yu, Y.J. Jiang, C.B. Jing, J.Y. Zhu, M. Zhu, Z.G. Hu, X.D. Tang, J.H. Chu, Phys. Chem. C 114 (2010) 11951–11957.
[16] W. Xie, Z. Yang, H. Chun, Ind. Eng. Chem. Res. 46 (2007) 7942–7949.
[17] S. Wang, X. Li, J. Zhang, J. Phys. Conf. Ser. 188 (2009) 012017–12024.
[18] R.S. Thompson, D. Li, C.M. Witte, J.G. Lu, Nano Lett. 9 (2009) 3991–3995.
[19] J.L. Liu, F.X. Xiu, L.J. Mandalapu, Z. Yang, Proc. SPIE 6122 (2007) 61220H–61227H.
[20] X. Fang, J. Li, D. Zhao, D. Shen, B. Li, X. Wang, J. Phys. Chem. C 113 (2009) 21208–21212.
[21] X.J. Liu, X.Y. Zhu, C. Song, F. Zeng, F. Pan, J. Phys. D: Appl. Phys. 42 (2009) 035004–35007.
[22] A. Singhal, S.N. Achary, J. Manjanna, S. Chatterjee, P. Ayyub, A.K. Tyagi, J. Phys. Chem. C 114 (2010) 3422–3430.
[23] T. Bulsgen, M. Hilgendorff, S. Irsen, F. Wilhelm, A. Rogalev, D. Goll, M. Giersig, J. Phys. Chem. C 112 (2008) 2412–2417.
[24] C. Xu, K. Yang, Y. Liu, L. Huang, H. Lee, J. Cho, H. Wang, J. Phys. Chem. C 112 (2008) 19236–19241.
[25] S.H. Lee, S.H. Han, H.S. Jung, H. Shin, J. Lee, J.H. Noh, S. Lee, I.S. Cho, J.K. Lee, H. Shin, J. Phys. Chem. C 114 (2010) 7185–7189.
[26] B. Gupta, A. Jain, R.M. Mehra, J. Mater. Sci. Technol. 26 (2010) 223–227.
[27] S.H. Jeong, J.W. Lee, S.B. Lee, J.H. Boo, Thin Solid Films 435 (2003) 78–82.
[28] O. Lupan, S. Shishiyanu, V. Ursaki, H. Khallaf, L. Chow, T. Shishiyanu, V. Sontea, E. Monaico, S. Railean, Sol. Energy Mater. Sol. Cells 93 (2009) 1417–1422.
[29] K. Nishizono, M. Okada, M. Kamei, D. Kikuta, K. Tominaga, Y. Ohno, Appl. Phys. Lett. 84 (2004) 3996–3998.
[30] J.S. Na, Q. Peng, G. Scarel, G.N. Parsons, Chem. Mater. 21 (2009) 5585–5593.
[31] O. Lupan, L. Chow, G. Chai, B. Roldan, A. Naitabdi, A. Schulte, H. Heinrich, Mater. Sci. Eng. B 145 (2007) 57–66.
[32] V.V. Ursakia, O.I. Lupan, L. Chow, I.M. Tiginyanu, V.V. Zalamai, Solid State Commun. 143 (2007) 437–441.
[33] S. Suwanboon, P. Amornpitoksuk, A. Haidoux, J.C. Tedenac, J. Alloys Compd. 462 (2008) 335–339.
[34] N.P. Dasgupta, S. Neubert, W. Lee, O. Trejo, J.R. Lee, F.B. Prinz, Chem. Mater. 22 (2010) 4769–4775.
[35] N.R. Yogamalar, R. Srinivasan, A. Chandra Bose, Opt. Mater. 31 (2009) 1570–1574.
[36] V. Biju, S. Neena, V. Vrinda, S.L. Salini, J. Mater. Sci. 43 (2008) 1175–1180.
[37] N.R. Yogamalar, R. Srinivasan, A. Vinu, K. Ariga, A. Chandra Bose, Solid State Commun. 149 (2009) 1919–1923.
[38] L. Xiao-bo, S. Hong-Lie, Z. Hui, L. Bin-bin, Trans. Nonferrous Met. Soc. China 17 (2007) s814–s817.
[39] H. Van Cong, S. Charar, S. Brunet, Phys. Status Sol. B 147 (2006) 253–258.
[40] J.G. Lu, S. Fujita, T. Kawaharamura, H. Nishinaka, Y. Kamada, T. Ohshima, Z.Z. Ye, Y.J. Zeng, Y.Z. Zhang, L.P. Zhu, H.P. He, B.H. Zhao, J. Appl. Phys. 101 (2007) 083705–83707.
[41] P. Banerjee, W.J. Lee, K.R. Bae, S.B. Lee, G.W. Rubloff, J. Appl. Phys. 108 (2010) 043504–43507.
[42] K.H. Tam, C.K. Cheung, Y.H. Leung, A.B. Djurisˇicĭ, C.C. Ling, C.D. Beling, S. Fung, W.M. Kwok, W.K. Chan, D.L. Phillips, L. Ding, W.K. Ge, J. Phys. Chem. B 110 (2006) 20865–20871.
[43] S.K. Pand, N. Singh, J. Hooda, C. Jacob, Cryst. Res. Technol. 43 (2008) 751–755.
[44] Y.G. Wanga, S.P. Laua, X.H. Zhang, H.H. Hngc, H.W. Lee, S.F. Yua, B.K. Taya, J. Cryst. Growth 259 (2003) 335–342.
[45] D.C. Altamirano-Juárez, G. Torres-Delgado, R. Castanedo-Pérez, O. Jiménez-Sandoval, J. Márquez-Marín, S. Jiménez-Sandoval, Superficies y Vacío 13 (2001) 66–68.
[46] N.R. Yogamalar, S. Anitha, R. Srinivasan, A. Vinu, K. Ariga, A. Chandra Bose, J. Nanosci. Nanotechnol. 9 (2009) 5966–5972.
[47] S. Liufu, H. Xiao, Y. Li, Powder Technol. 145 (2004) 20–24.